Supplementary information

for

3D printed triply periodic minimal surfaces as advanced structured packings for solvent-based CO_2 capture

Nathan C. Ellebracht[a], Pratanu Roy[a], Thomas Moore[b], Aldair E. Gongora[b], Diego I. Oyarzun[b], Joshuah K. Stolaroff[c], Du T. Nguyen[b,*]

[a]Physical and Life Sciences Directorate, Lawrence Livermore National Laboratory, Livermore, California 94550, USA
[b]Engineering Directorate, Lawrence Livermore National Laboratory, Livermore, California 94550, USA
[c]Mote, Inc, Los Angeles, California 90034, USA

1 Supplementary information

1.1 3D-printed structured packing surfaces and other TPMS

Table S1. Basic physical properties and defining equations of packing structures included in this work.

Packing	SSA (m^2 m^{-3})	Void fraction	Defining equation
Schwarz-P	250	0.746	$\cos(x) + \cos(y) + \cos(z) = 0$
Schwarz-D	250	0.771	$sin(x)cos(y) + sin(y)cos(z) + sin(z)cos(x) = 0$
Gyroid	250	0.779	$\sin(x)\sin(y)\sin(z) + \sin(x)\cos(y)\cos(z) + cos^{2}(x)sin^{2}(y)cos^{2}(z) + cos$
250Y	250	0.942	*N/A, custom CAD structure*

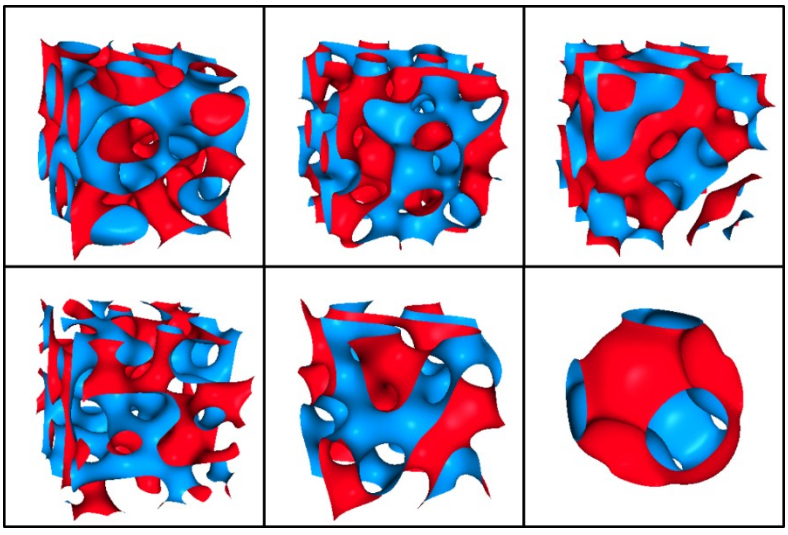

Figure S1. Depictions of six TPMS geometry examples. Several additional TPMS structured packings were screened via simulations to identify trends which can identify optimum geometries for gas-liquid transport applications.

1.2 Maldistribution quantification

We utilized Ripley's K function[1,2] to quantify maldistribution as a single value from outlet liquid distribution data from structured packing geometries, collection of which is described in the Methods section. To establish this maldistribution metric protocol, we artificially rearranged the location of the collected liquid to result in qualitatively 'grouped' and 'spread' collections (Figure S2). In each case, the coefficient of variation (CoV) is identical since no spatial information is used for a CoV measurement. However, a maldistribution analysis using Ripley's K function correctly differentiates the various configurations.

Using the CFD model, we examined the fluid distributions of 10 total TPMS structures (P2YSV2P2Y_{yzss}, $JI_{xxx}I_{zx}IP2I_z$, $PJP2_{xxx}P_zP_{zxx}$, Y_{yxx}, S_s, Schwarz-D, IWP, Gyroid, PP_{xxx}, Schwarz-P) that spanned a broad range of geometric properties to determine if any geometric correlation exists (Figure S3). After comparing both CoV and Ripley's K function to a variety of geometric properties, we found that across these 10 structures a correlation exists between the unit cell hydraulic diameter and the liquid maldistribution (Figure S3). Since each of the structures were normalized to have a specific surface area of 250 m^2/m^3, the packings based on TPMS structures with larger unit cell hydraulic diameters had more unit cells within a given volume. Each unit cell added enables a 'split' in the flow path and which may have helped improve the liquid distribution.

The potential improvement due to additional number of unit cells was examined by performing a series of simulations for the Gyroid geometry and varying the specific surface area of the overall packing (Figure S4). As the specific surface are increases, more unit cells are introduced into the volume. We found that as the specific surface area increased, the maldistribution improved up to 250 m^2/m^3. After that point, the maldistribution worsened. This is likely due to the constraint that the wall thicknesses were held at a constant 2 mm thickness. At the higher specific surface areas, there was a smaller void fraction for the liquid and gas to flow resulting in more flooded regions and worsening the maldistribution.

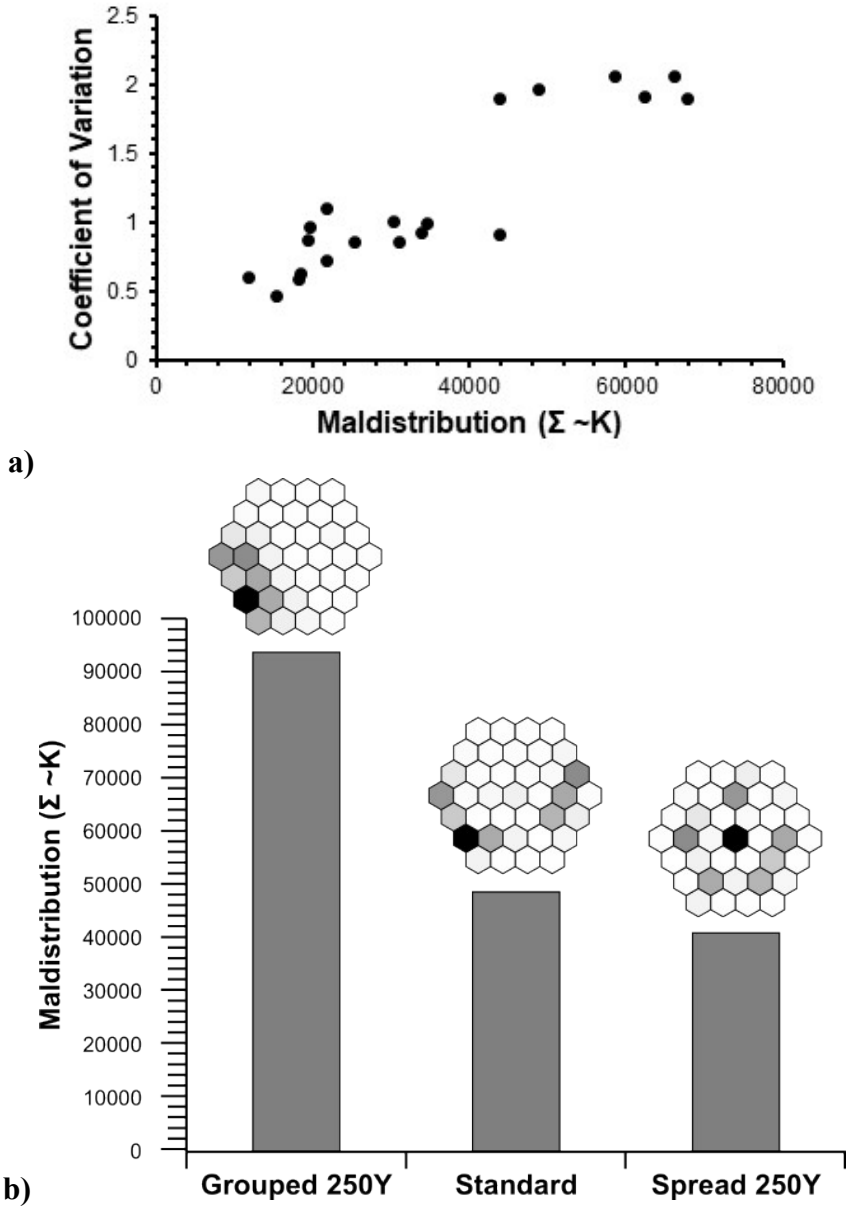

Figure S2. a) Comparison of CoV and maldistribution. A range of varying patterns were examined with different CoV and maldistribution values. In a general sense, a correlation exists. However, the maldistribution values can provide further insight into the fluid distribution by incorporating spatial information. b) Three different fluid distributions were compared which have the same CoV. Using Ripley's K function extended to greyscale values, the spatial grouping of the different distributions could be measured.

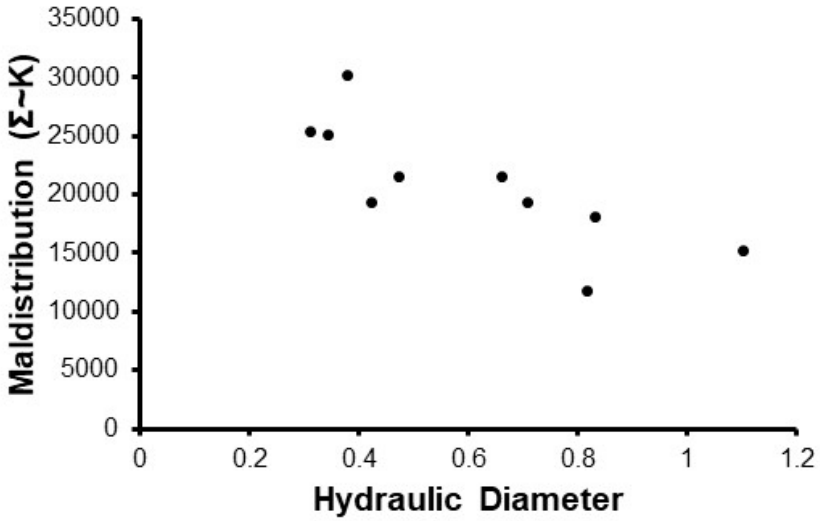

Figure S3. Maldistribution of TPMS geometries. A total of 10 different TPMS geometries were examined based on how well they distributed liquid. A general correlation was found between maldistribution and the unit cell hydraulic diameter of the TPMS geometries.

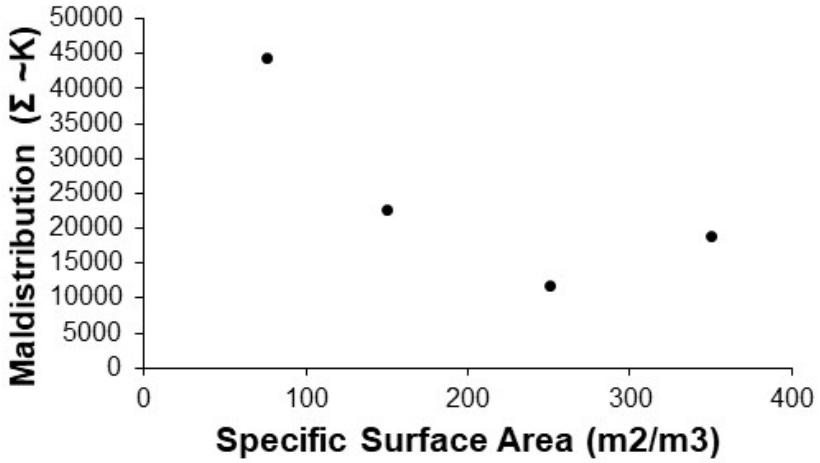

Figure S4. Maldistribution vs. specific surface area. Several Gyroid structured packings with differing specific surface areas were modeled and their maldistributions measured. In general, as the specific surface area increased, the maldistribution decreased. However, once the specific surface area increased further, the void fraction available for liquid and gas flow decreased. As a result, more liquid could pool and worsen the liquid distribution of the packing.

1.3 Two phase flow distribution videos

Refer to additional video files available in the Supplementary Information. "250Y_Schwarz-D_CFD.mp4" is a side-by-side comparison of developing liquid flow and distribution in computational fluid dynamics simulations. "250Y_flow_visualization.mp4" and "Schwarz-D_flow_visualization.mp4" are individual videos of liquid flow visualization tests using dyed water in 250Y and Schwarz-D.

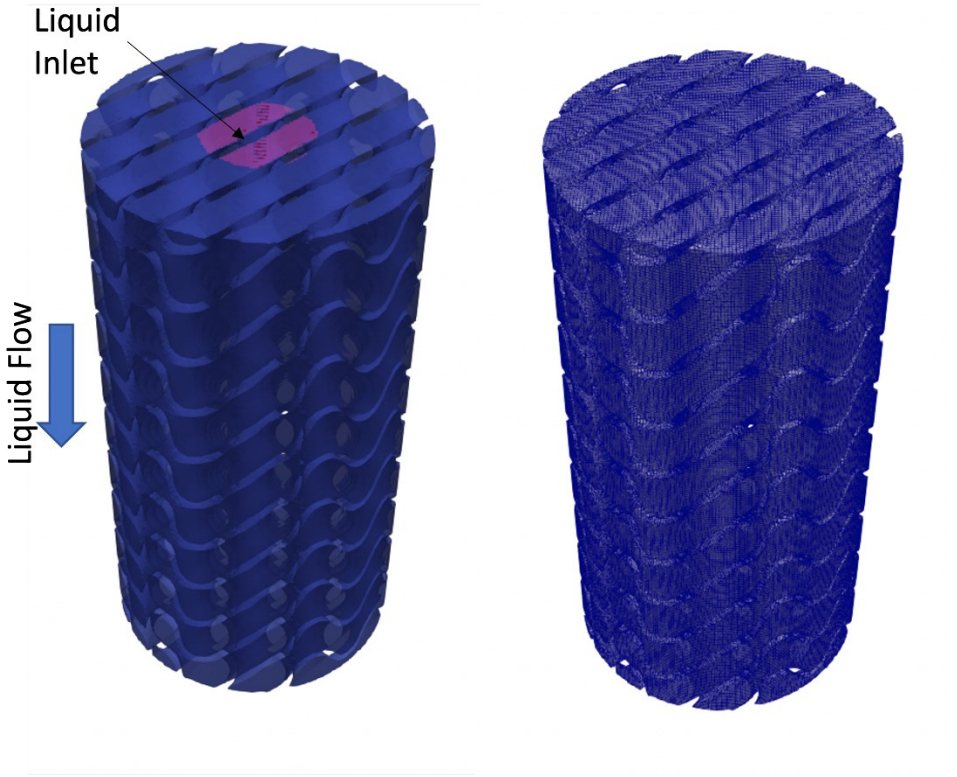

Figure S5. Representative structured packing geometry as imported into and meshed (right) in OpenFOAM. The structure pictured here is Schwarz-D.

Table S2. Boundary conditions for two-phase flow simulations

Boundary	Boundary Conditions
Liquid inlet	Uniform velocity
Liquid outlet	Pressure outlet
Gas inlet	Fixed pressure
Walls	No slip with contact angle

1.4 Absorber operation experimental results and parameters

During transient absorber operation and across experiments with different packings, we maintained approximately equal inlet gas and liquid flow rates so the resulting flow velocities with Mellapak 250Y were marginally lower than those in the TPMS packings, which have lower void fractions. The raw and time-averaged measured data from representative absorption experiments are shown below.

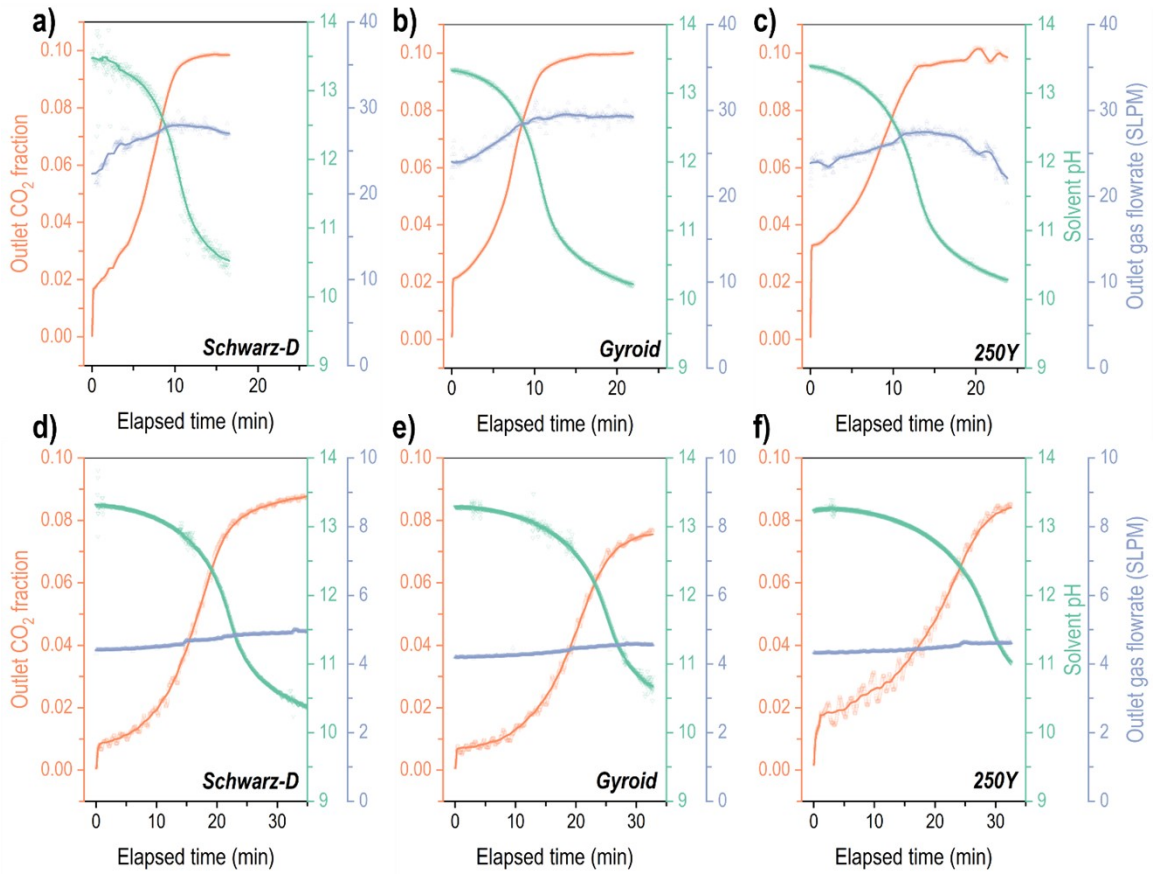

Figure S6. Batch absorber operation data for a–c) 'high' and d–f) 'low' flow carbon capture experiments. The feed gas was 10% CO_2 in N_2, and the recirculated solvent was aqueous NaOH. The pH at the liquid inlet (column top) as well as the CO_2 gas fraction and gas flow rate out were measured. Raw data are shown in hollow symbols (faint), and 30–60 s data moving averages (to account for sensor fluctuations) are depicted as solid lines. The absorber was run with three stacked 150 mm packing sections of the structure noted on each plot.

Table S3. Inlet liquid (capture solvent) and gas (10% CO_2) velocities for absorption operations. Gas velocities are calculated from a background inlet flow rate. Initial outlet flow is reduced as a significant fraction of the inlet CO_2 is removed from the gas stream.

	High flow		Low flow	
Packing	v_G (m s^{-1})	v_L (m h^{-1})	v_G (m s^{-1})	v_L (m h^{-1})
Schwarz-D	0.14	55	0.025	13
Gyroid	0.13	54	0.023	14
250Y	0.105	45	0.019	11

1.5 1D absorber model for experimental data fitting

To note, the effective interfacial areas for Gyroid and Schwarz-D were greater than the physical packing surface areas This is possible in two-phase flow, as the mass transfer area can be greatly enhanced by the convective transport mechanism and vigorous two-phase flow but may in part be a result of limitations of the simplified 1D model. For example, underestimated values of kinetic parameters from rate equations, taken from literature references of homogeneous reactions of CO_2 and KOH, could be balanced by slightly inflated interfacial areas.

Table S4. Best fit parameters from modeling for high flow and low flow absorber operation data determined via minimizing model error with an optimization function.

	High flow			Low flow		
Packing	k_L (mm s^{-1})	a_{eff} (m^{-1})	$k_L a_{eff}$ (s^{-1})	k_L (mm s^{-1})	a_{eff} (m^{-1})	$k_L a_{eff}$ (s^{-1})
Schwarz-D	0.142	415	0.059	0.150	155	0.023
Gyroid	0.193	330.	0.064	0.152	151	0.023
250Y	0.23	172	0.040	0.266	58.6	0.016

Table S5. Best fit parameters from modeling for high flow absorber operation data using different pH cutoff points. A cutoff of pH ≥ 12.5 was selected as model fit results tended to converge at lower pH cutoffs as they captured a wider range of solvent loading and pseudo-equilibrated absorber operational states from the experimental data.

	Cutoff: pH ≥ 12.5			Cutoff: pH ≥ 13		
Packing	k_L (mm s^{-1})	a_{eff} (m^{-1})	$k_L a_{eff}$ (s^{-1})	k_L (mm s^{-1})	a_{eff} (m^{-1})	$k_L a_{eff}$ (s^{-1})
Schwarz-D	0.142	415	0.059	0.210	368	0.077
Gyroid	0.193	330.	0.064	0.493	287	0.14
250Y	0.23	172	0.040	0.611	150.	0.092

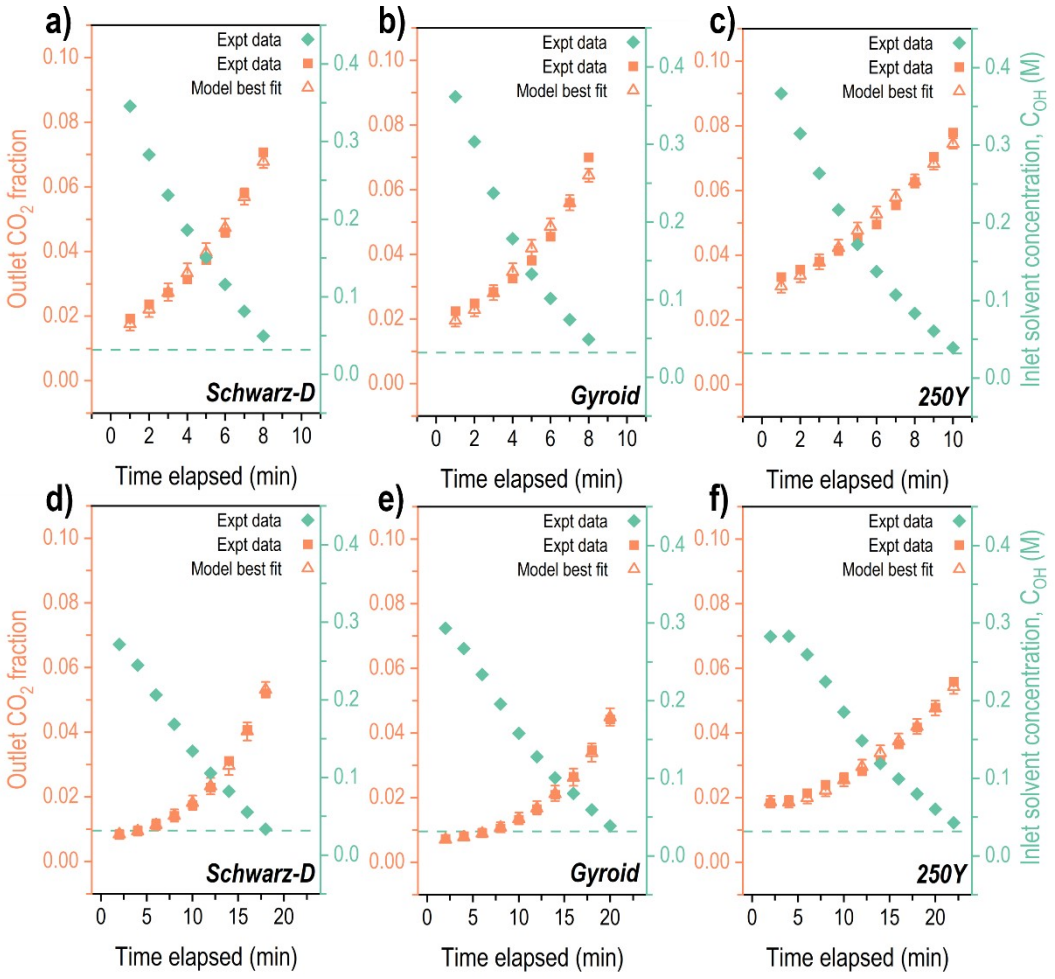

Figure S7. Select experimental data from a–c) high (one point per one minute)and d–f) low (one point per two minutes) flow absorber operations and resulting best fit modeled data (open symbols). Error bars on modeling results represent model fits with ±5% perturbed in k_L and a_{eff} best fit values. The packing type for each dataset is labeled on the plot. The dotted line represents the cutoff at pH = 12.5 for data pulled from experiments to be fit. The model used the experimental solvent concentration (C_{OH^-}) as an input and returned a predicted outlet CO_2 fraction to be compared to the experimentally measured value.

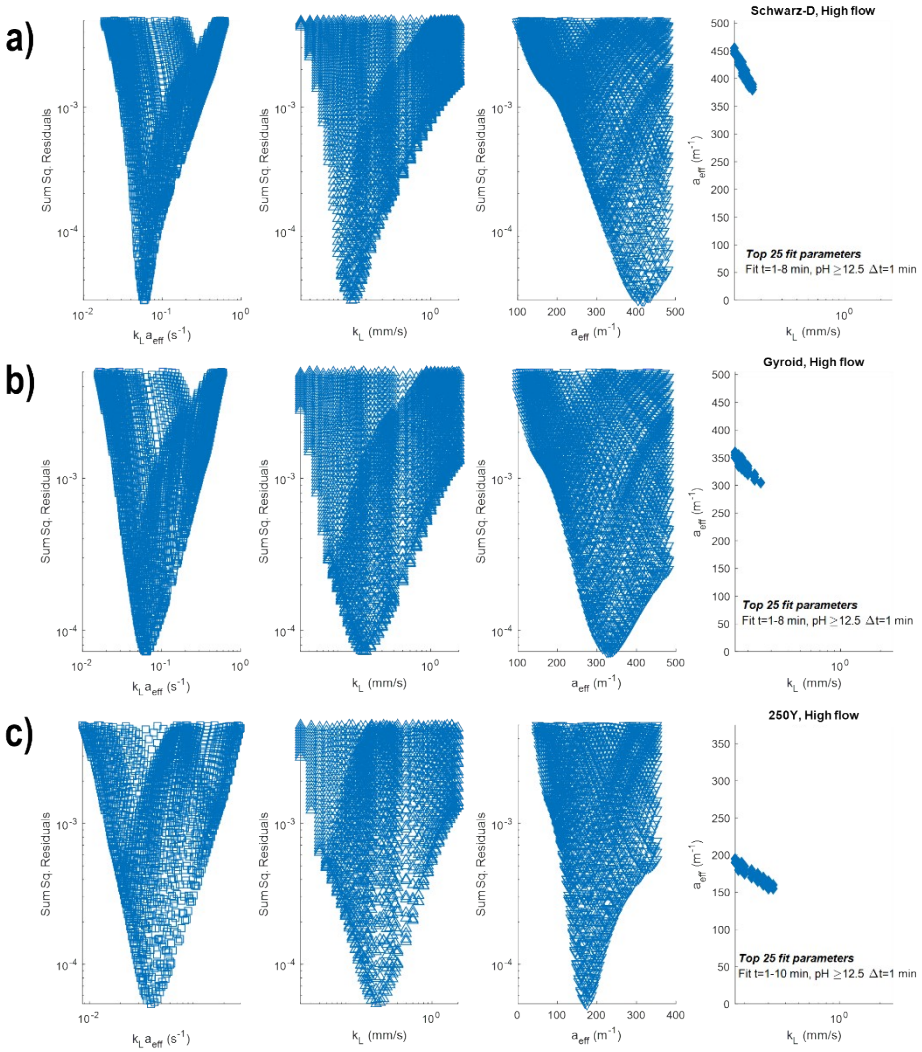

Figure S8. Model fitting residuals (sum of squares) in high flow experiments for a) Schwarz-D, high flow absorber data, b) Gyroid, high flow, and c) 250Y, high flow across a broad range of mass transfer coefficients, k_L (left middle) and effective interfacial areas, a_{eff} (right middle). The product of the two, $k_L a_{eff}$ (left) and top 25 fit parameter pairs (k_L, a_{eff}) (right) are also shown. Absolute best fits reported are based on a model optimization function; residuals shown here are demonstrative of fitting sensitivity to packing parameters.

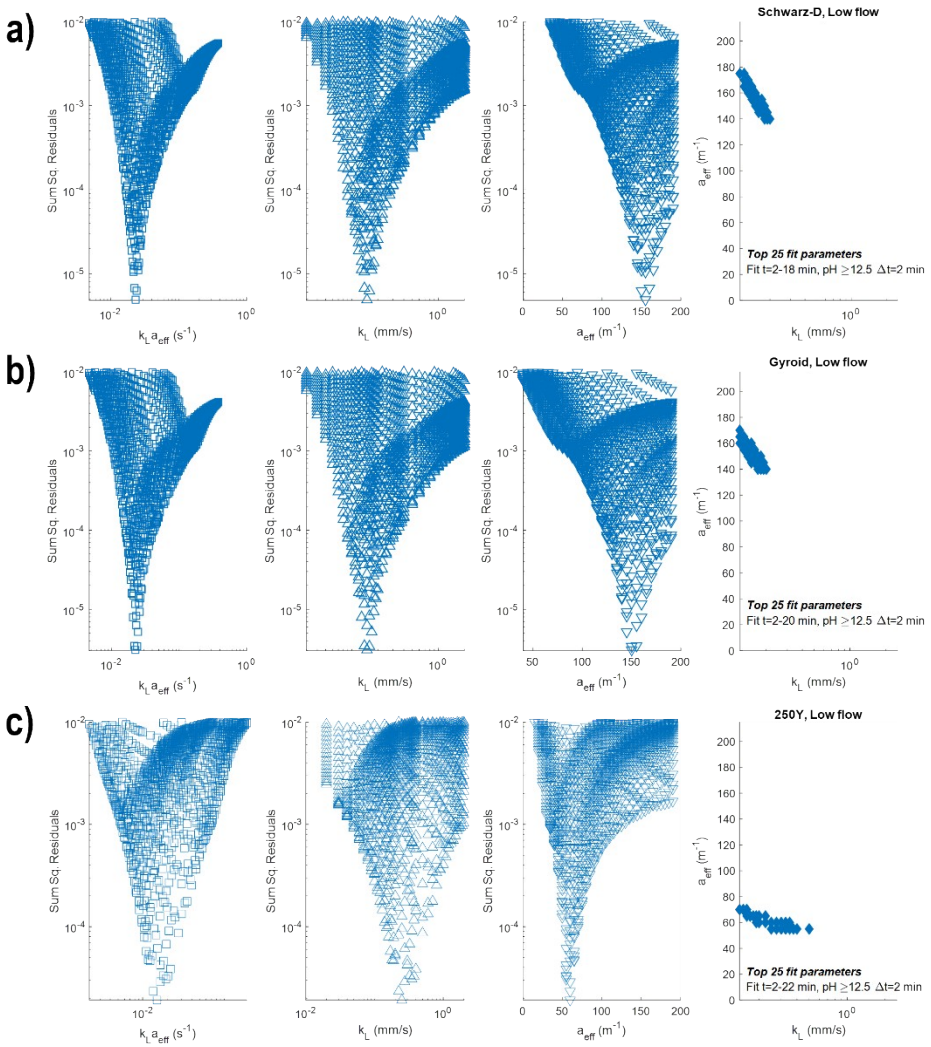

Figure S9. Model fitting residuals (sum of squares) in low flow experiments for a) Schwarz-D, high flow absorber data, b) Gyroid, high flow, and c) 250Y, high flow across a broad range of mass transfer coefficients, k_L (left middle) and effective interfacial areas, a_{eff} (right middle). The product of the two, $k_L a_{eff}$ (left) and top 25 fit parameter pairs (k_L, a_{eff}) (right) are also shown. Absolute best fits reported are based on a model optimization function; residuals shown here are demonstrative of fitting sensitivity to packing parameters.

Additional 1D model details

The full expression for the enhancement factor, as given by Wellek *et al.*,[3] is as follows:

$$E = 1 + \left(\frac{1}{(E_1 - 1)^{1.35}} + \frac{1}{(E_i - 1)^{1.35}} \right)^{-1/1.35}$$

where

$$E_1 = \frac{Ha}{\tanh Ha}$$

and

$$E_i = 1 + \frac{C_{OH-}}{z \cdot C_{CO2-GL}} \cdot \frac{D_{CO2,L}}{D_{OH,L}}$$

where $D_{CO2,L}$ is the liquid diffusion coefficient of CO_2 in water, $D_{OH,L}$ is the diffusion coefficient of hydroxide ions, z is the stoichiometric coefficient, and $C_{CO2\text{-}GL}$ is the concentration of CO_2 as the gas–liquid interface determined by $P_{CO2}H$.

Due to experimental constraints in measuring internal solvent temperature, the model assumed a constant temperature of 25 °C. Gas and liquid flow rates were relatively high, which minimized temperature change by rapidly dissipating generated heat. A full energy balance for the system was not performed, and temperature change could be a factor that could help improve model fitting shape.

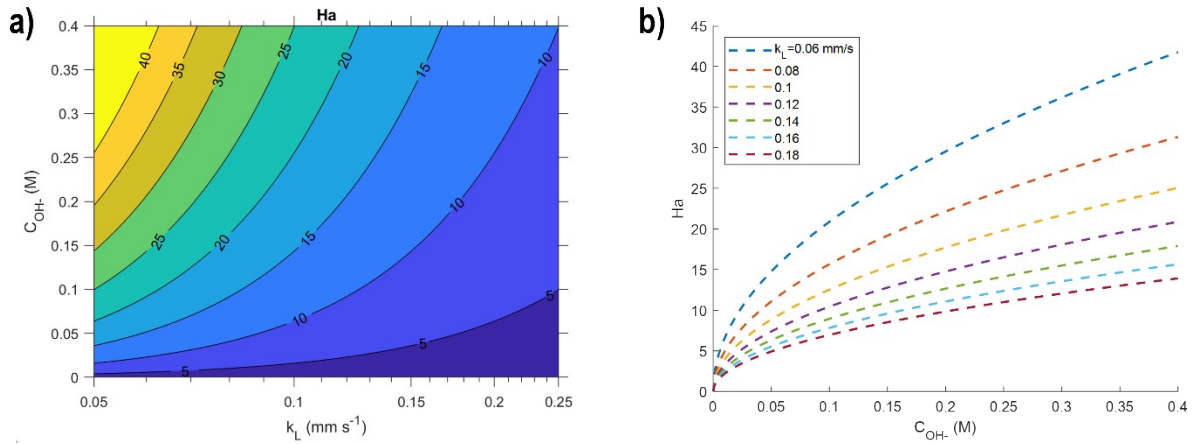

Figure S10. a) A contour plot of Hatta numbers, the non-dimensional ratio of liquid phase reaction rate to liquid mass transfer, as a function of hydroxide solvent concentration (C_{OH-}) and liquid mass transfer coefficient (k_L) at T = 25 °C. b) An alternative representation of Ha as a function of solvent concentration for various liquid mass transfer coefficients. Each line is effectively a vertical slice of the contour plot in (a).

Photopolymer stability to alkaline solutions

Coupons (10 mm square) of photopolymer acrylate resin (Formlabs "Clear resin") were printed and cured in the same manner as the printed structured packings. The coupons were submerged at room temperature in 20 mL of two different representative CO_2 solvents: 2 N sodium hydroxide (aqueous inorganic) and neat amino-2-propanol (amine-based organic) and stored for 90 days. Before and after solvent exposure, the chemical surface compositions were analyzed via attenuated total reflection Fourier transform infrared spectroscopy (ATR-FTIR) (Bruker Alpha II compact FT-IR spectrometer). Coupons were washed with DI water prior to measurement. As seen in Figure S11, negligible chemical changes were observed in the FT-IR spectra after treatment with either solvent, indicating reasonable chemical stability to typical strong alkaline liquid CO_2 solvents. No observable physical changes nor change in contact angle with water were observed.

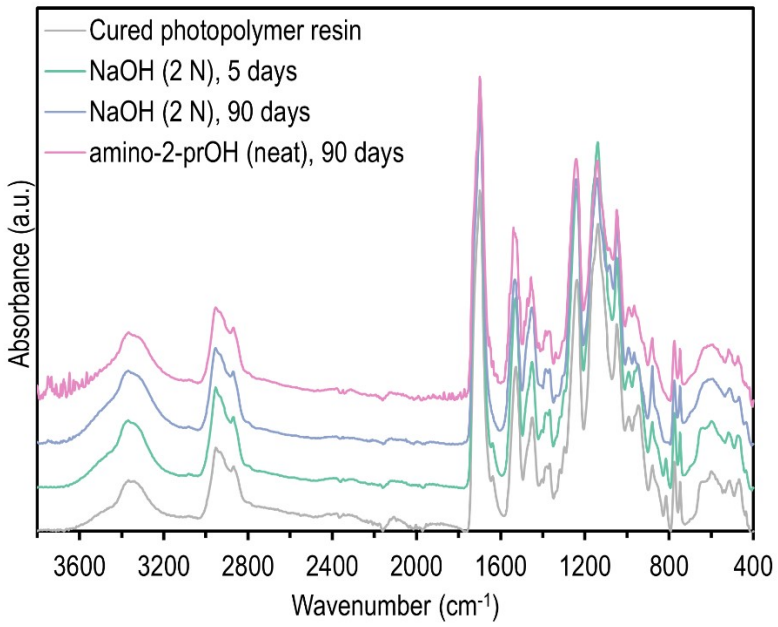

Figure S11. ATR-FTIR absorbance spectra of cured photopolymer acrylate resin (Formlabs, Clear resin) before and after short- and long-term exposure to inorganic (NaOH) and organic (amino-2-propanol) alkaline liquid CO_2 solvents. Spectra are vertically offset for visual clarity.

2 References

1. Amgad, M., Itoh, A. & Tsui, M. M. K. Extending Ripley's K-Function to Quantify Aggregation in 2-D Grayscale Images. *PLOS ONE* **10**, e0144404 (2015).
2. Dixon, P. M. Ripley's K Function. in *Encyclopedia of Environmetrics* (John Wiley & Sons, Ltd, 2013). doi:10.1002/9780470057339.var046.pub2.
3. Wellek, R. M., Brunson, R. J. & Law, F. H. Enhancement factors for gas-absorption with second-order irreversible chemical reaction. *The Canadian Journal of Chemical Engineering* **56**, 181–186 (1978).